

Shape Estimation of Continuum Robots via Modal Parameterization and Dual Extended Kalman Filter

Guoqing Zhang and Long Wang

Abstract—The equilibrium shape of a continuum robot is resulted from both its internal actuation and the external physical interaction with a surrounding environment. A fast and accurate shape estimation method (i) can be used as a feedback to compensate for more accurate motion; and (ii) can reveal rich information about physical interactions (e.g. instrument-anatomy contacts / forces during a surgery).

From a prior work that demonstrated an offline calibration of continuum robots, we adopt its shape modal representation and error propagation models that include identification Jacobians. In this work, we present an iterative observer approach to enable online shape estimation. We develop a dual Extended Kalman Filter (EKF) to estimate both the robot state and the shape modal parameters. The dual EKF provides robust estimation on (i) the configuration space variables that are controllable and driven by internal actuation; and (ii) the modal coefficients representing homotopies of shape families that are governed by the physical interactions with the environment. We report results from simulation studies in this work, and plan to investigate methods in the future to use the proposed approach for predicting physical interactions.

I. INTRODUCTION

Inspired by biological features such as an elephant’s trunk or an octopus’s tentacles, continuum robots are an unconventional class of robots that have inherent large degrees of flexibility, underactuation, and compliance. Such “soft” features allow them to have safe physical interactions with the environments [1]. With recent advances in instrument miniaturization, continuum robot designs have been widely used in many minimally invasive surgery applications [2], [3], and their advantages are further leveraged for safe manipulation and for access to deep anatomy.

Shape modeling, sensing, and estimation of continuum robots is challenging and remains an open problem. The equilibrium shape of a continuum robot is resulted from both its *internal* actuation and the *external* physical interaction with a surrounding environment. The internal actuation problem is difficult due to the uncertainties and nonlinearities caused by flexible conduit friction, internal loading distribution along the continuous slender body, and cross-sectional flexural rigidity. The external physical interaction is almost unmodelable because of the large number of underactuated degrees of freedom (infinite in theory) of the continuous body. Yet, the equilibrium shape is the only accessible geometric observation that one could obtain to reveal the rich

This work was supported in part by USDA-NIFA Grant No. 2021-67022-35977.

G. Zhang and L. Wang are with the Department of Mechanical Engineering, Stevens Institute of Technology, New Jersey, NJ, 07030, USA, e-mail: long.wang@stevens.edu

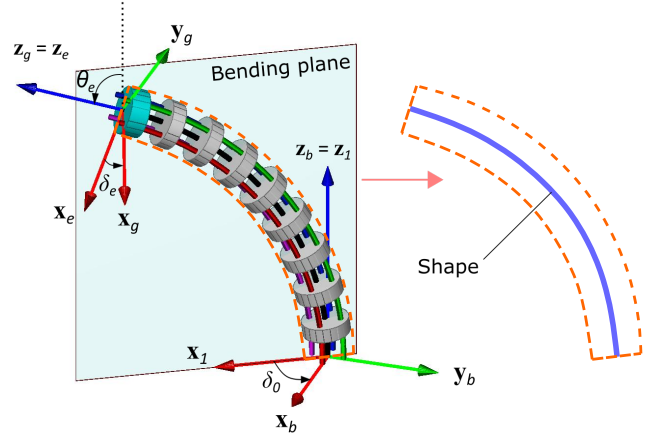


Fig. 1: Illustration of estimating and extracting shape using limited measurements and modeling knowledge

information hidden in the aforementioned internal actuation process and external physical interaction process.

We focus on the shape estimation problem for continuum robots. Specifically, as illustrated in Fig. 1, we are interested in the problem of estimating and extracting shape information with the following considerations:

- 1) only limited position and/or orientation measurements are provided at the sensor location(s)
- 2) the estimates of shape are in the format of compact parameterization
- 3) the kinematics model is embedded into the estimation problem

The consideration (1) makes the proposed approach accessible for researchers to adopt with off-the-shelf sensors: Electro-Magnetic sensors, Inertia Measurement Unit (IMU) sensors, and computer vision algorithms to track features. The considerations (2, 3) enables development of observer-based controllers for continuum robots in the future. As follows, we discuss the two main contributions of this work.

A. Online Stochastic Shape Estimation

In prior work [4], the authors presented an offline and batch process to calibrate the shape parameters without considering dynamic process noise.

In this work, we develop an EKF method to estimate the shape for online usage that consumes continuously obtained measurements and that optimizes stochastic information (covariance matrices of estimates).

B. Dual Estimation of State and Shape Parameters

We leverage the compact modal shape representation in [4], conveniently separating (i) the controllable configuration space variable - the **state**; and (ii) the modal coefficients that parameterize the boundaries of a homotopy of curves under the same external loading condition - the **parameters**.

The proposed dual EKF method estimates both the state and the parameters, enabling future controls approaches that can take advantage of both estimates.

II. RELATED WORK

Related work on shape modeling primarily includes (i) the geometric-based approaches and (ii) the mechanics-based approaches. For the first group, we will discuss the constant curvature methods and the variable curvature methods. For the second group, we will discuss the Cosserat Rod Theory methods and pseudo-rigid body based methods.

A. Constant Curvature Models

assume that the continuum robot segments articulate in constant curvature shape (circular arc). Constant curvature models are reasonable approximates for ideal situations such as uniform mass/material distribution, frictionless transmission, and free from external loading. Constant curvature approaches are simplified, with available analytical solutions, and can be adopted and deployed easily. They have enabled continuum robots for a variety of practical applications such as surgery [5–8], field [9], underwater [10], and aerial [11]. The use of constant curvature models can be found in diverse examples of mechanical structures: tendon-drive [7], multi-backbone [12], and concentric tubes [6], [8].

B. Variable Curvature

In recent works, researchers have presented promising methods for variable curvature methods for shape modeling to address the limitations in constant curvature methods. Examples include modal-based methods [4], [13–15], Bézier curves [16–18], and Pythagorean-Hodograph curves [19], [20].

Modal-based kinematics describes shape functions to a modal form, capturing the continuum robot geometric characteristic [14]. Inspired by [14], in prior work [4], [15], the authors used a homotopy of backbone curves to define the continuum robot's shape family and then adopted an interpolation variable to serve as the configuration space of the robot.

C. Cosserat Rod Theory

solves the equilibrium shape of a continuum robot by considering the underlying mechanics and by solving positional, force, moment boundary conditions [21–25]. While also describing shape as variable curvature functions, Cosserat rod theory methods are different from the geometric-based approaches above in that they embed the underlying physics equations, at a cost of having to solve boundary condition partial differential equations. Recent progress have shown promising real-time usage [22].

D. Psuedo-rigid Body

approximates the central backbone shape of continuum robots as a series of rigid links connected by torsion springs [26–29]. While also solving the mechanics equations, compared to Cosserat rod theory methods, the smaller number and simpler spring assumption of the discrete joints make such methods attractive in practice.

E. Estimating Force via Shape

has been a promising research direction in continuum robots. Examples include contact detection by capturing the instantaneous screw axis [30], [31] and force estimation from shape using fiber Bragg grating (FBG) sensors [32].

III. PROBLEM FORMULATION

We formulate the online shape estimation problem as:

- Given the *kinematics model* and the *measurement model*, develop a *recursive estimation method* to obtain the optimal estimate of the robot state and the shape parameters with continuous measurements.

The kinematics model is adopted from [4] and briefly reviewed in III-A. The measurement model is described in III-B. The recursive estimation method is briefly introduced in III-C.

A. Kinematics Model

1) *Kinematics Nomenclature*: Many researchers (e.g. [4]) use configuration space to characterize the shape of a continuum segment. Figure 1 illustrates the configuration space variables of a single-segment continuum robot example, with all of its frames defined in Table I.

One configuration space variable is usually chosen to indicate the in-plane bending status, which corresponds to the angle θ_e in the example shown in Fig. 1. The bending angle θ_e is defined as a rotation angle from \mathbf{z}_1 to \mathbf{z}_g around \mathbf{y}_1 based on right-hand rule. Such bending configuration status variable, θ_e , was abstracted and formulated to an shape interpolation variable t in [4]. We adopt the same formulation and explain in details later.

The other configuration space variable can be chosen to describe the bending plane, which corresponds to angle δ in Fig. 1. In this paper, we assume the continuum segment

TABLE I: Frame Nomenclature in Kinematics

Symbol	Description
Frame $\{\mathbf{F}\}$	designates a right-handed frame with unit vectors $\hat{\mathbf{x}}_f, \hat{\mathbf{y}}_f, \hat{\mathbf{z}}_f$ and point \mathbf{f} as its origin.
Frame $\{\mathbf{B}\}$	defines the base frame with \mathbf{b} located at the center of the base disk, $\hat{\mathbf{x}}_b$ passing through the first secondary backbone and $\hat{\mathbf{z}}_b$ perpendicular to the base disk.
Frame $\{\mathbf{1}\}$	characterizes the bending plane and is obtained by a rotation of $(-\delta_0)$ about $\hat{\mathbf{z}}_b$ from Frame $\{\mathbf{B}\}$
Frames $\{\mathbf{E}\}$ & $\{\mathbf{G}\}$	Frame $\{\mathbf{G}\}$ and Frame $\{\mathbf{E}\}$ are attached to the end disk. The x-axis of $\{\mathbf{E}\}$ is the intersection of the bending plane and the top surface of the end disk. Frame $\{\mathbf{G}\}$ is obtained by a rotation (δ_e) about $\hat{\mathbf{z}}_e$ from $\{\mathbf{E}\}$.

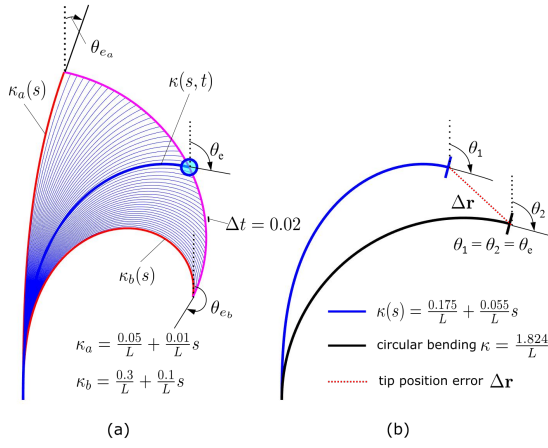


Fig. 2: Illustration of shape interpolation

bends without torsional twist along the central backbone. Thus, the bending plane angle is not a function of the backbone length, which yields $\delta = \delta_0 = \delta_e$.

2) Shape Assumption: In practice, the equilibrium bending shape of a continuum robot deviates from constant curvature model. Bearing in mind that the constant curvature assumption corresponds to a 0th-order polynomial in the curvature space, it is extended a 1st-order polynomial in this work. At a given bending state (due to internal and external loading conditions), the curvature function along the backbone arc length s can be described as:

$$\kappa(s) = m_1 + m_2 s, \quad s \in [0, L] \quad (1)$$

thereby, the bending angle θ_e is integrated as:

$$\theta_e(l) = \theta_0 + \int_0^l \kappa(s) \, ds, \quad l \in [0, L] \quad (2)$$

where θ_0 represents the bending angle at $s = 0$, m_1 and m_2 are the modal factors, l is the length of sensor installation, and L is the maximum segment length.

According to (2), the bending shape is driven by the time-variant modal factors, m_1 and m_2 . However, (2) does not decouple the shape description based on internal actuation and external loading conditions. In addressing this limitation, the representation proposed in [4] is particularly useful, in that,

- (i) it introduced “boundaries” or “generators” for a homotopy of curves
- (ii) it introduced an interpolation variable to describe the level of bending

For item (i), the curvature functions (the shape generator functions) $\kappa_a(s)$ and $\kappa_b(s)$ capture the two boundaries of a homotopy, described as:

$$\kappa_a(s) = \mathbf{a}^\top \boldsymbol{\eta}, \quad \kappa_b(s) = \mathbf{b}^\top \boldsymbol{\eta}, \quad \boldsymbol{\eta}(s) = [s^0, s^1]^\top \quad (3)$$

where $\mathbf{a}, \mathbf{b} \in \mathbb{R}^{2 \times 1}$ are vectors of modal factors and $\boldsymbol{\eta}(s)$ is a vector of modal functions.

For item (ii), we adopt the interpolation scheme in [4] and use a variable $t \in [0, 1]$ to capture a specific bending shape

from a homotopy. The interpolated curvature function $\kappa(s, t)$ is described below and depicted in Fig. 2):

$$\kappa(s, t) = t\kappa_b(s) + (1 - t)\kappa_a(s) \quad t \in [0, 1], s \in [0, L] \quad (4)$$

The following equation can be obtained by directly integrating the interpolated curvature function, resulting a convenient relationship for bending angle interpolation:

$$\theta_e = \theta_0 + \int_0^L \kappa(s, t) \, ds = \theta_{e_a} + t(\theta_{e_b} - \theta_{e_a}) \quad (5)$$

where θ_{e_a} and θ_{e_b} are bending angles corresponding to the shape generators (boundaries).

3) Definition of the State and the Parameters: The shape interpolation representation in [4] allows the convenient separation of robot state and shape parameters. The robot state is strongly correlated with its actuation actions. And we hypothesize that the shape parameters (the boundaries of the homotopies) are driven by factors that are independent from actuation schemes, which may include external force loading.

The robot state is thereby represented using the configuration space variables that include the shape interpolation parameter t and the bending plane angle δ as:

$$\boldsymbol{\psi} \triangleq [t, \delta]^\top \quad (6)$$

We limit the scope of this work to in-plane bending motion, and we further reduce the robot state to only include the shape interpolation parameter t , and the robot state becomes \mathbf{x} , defined as:

$$\mathbf{x} \triangleq t \quad (7)$$

The shape parameter vector, \mathbf{w} , is then defined as:

$$\mathbf{w} \triangleq [l, \mathbf{a}^\top, \mathbf{b}^\top]^\top, \mathbf{w} \in \mathbb{R}^{5 \times 1} \quad (8)$$

where l is the arc length where a sensor is installed, $\mathbf{a}, \mathbf{b} \in \mathbb{R}^{2 \times 1}$ are the modal factors in (3).

The robot state \mathbf{x} and shape parameter vector \mathbf{w} determine bending shape. The shape estimation problem can be decomposed as: the state estimation for the robot state \mathbf{x} and the parameter estimation for \mathbf{w} .

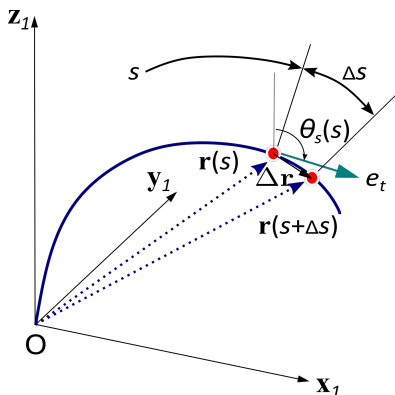


Fig. 3: Schematic of in-plane bending kinematics

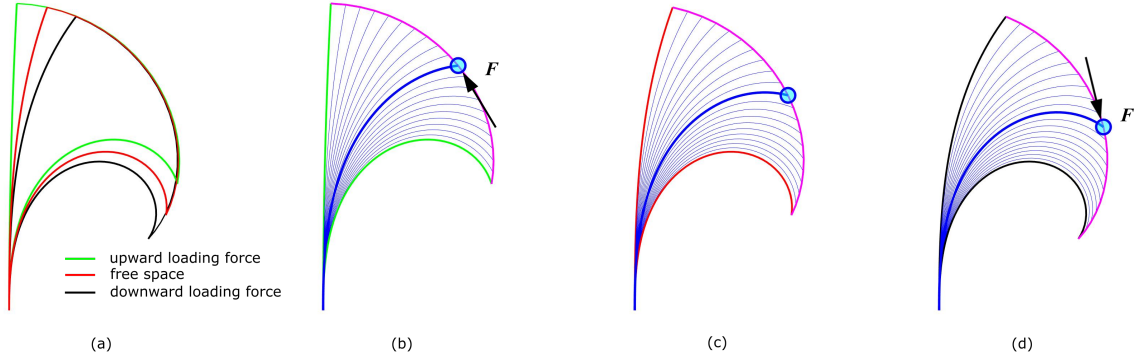


Fig. 4: Illustration of physical interactions governing different homotopies of shape families: (a) overlapped parent curves under different loading conditions; (b) a homotopy of curves with upward loading force at tip; (c) a homotopy of curves under free space; and (d) a homotopy of curves with downward loading force at tip

4) *In-plane Bending Kinematics*: Figure 3 shows the derivation of the in-plane bending kinematics. Let $\mathbf{r}(s)$ be the position at curve length s . We then consider the infinitesimal position change caused by Δs as:

$$\Delta\mathbf{r} = \mathbf{r}(s + \Delta s) - \mathbf{r}(s) \quad (9)$$

The tangent unit vector is derived as:

$$\mathbf{e}_t \triangleq \frac{d\mathbf{r}}{ds} = \lim_{\Delta s \rightarrow 0} \frac{\Delta\mathbf{r}}{\Delta s} = [s_{\theta_s(s)}, 0, c_{\theta_s(s)}]^\top \quad (10)$$

Then, the position vector $\mathbf{r}(s)$ is derived as:

$$\begin{aligned} \mathbf{r}(s) &\triangleq [p_x(s), p_y(s), p_z(s)]^\top \\ &= \int_0^s (d\mathbf{r}/d\tau) d\tau \quad s \in [0, L] \quad (11) \\ &= \int_0^s [s_{\theta_s(\tau)}, 0, c_{\theta_s(\tau)}]^\top d\tau \end{aligned}$$

$$\theta_s(s) = \int_0^s \kappa(\tau, t) d\tau \quad s \in [0, L] \quad (12)$$

B. Measurement Model

We choose a planar measurement format in this work and plan to extend to 6-dimensional measurement in future work. By combining the in-plane position and the bending angle, We can formulate the measurement model as a function of shape state \mathbf{x} and shape parameter \mathbf{w} :

$$\mathbf{y}_p \triangleq \mathbf{h}_p(\mathbf{x}, \mathbf{w}) = [{}^1p_x(l), {}^1p_z(l), \theta_e(l)]^\top \quad (13)$$

where $l \in [0, L]$ is the sensor install location along the backbone, $({}^1p_x, {}^1p_z)$ indicates the \mathbf{x} and \mathbf{z} coordinates of the sensor in Frame {1}, and θ_e is the in-plane bending angle.

To facilitate the shape estimation framework, the identification Jacobian \mathbf{J}_w and geometric Jacobian \mathbf{J}_x are defined:

$$\mathbf{J}_w \triangleq \frac{\partial \mathbf{h}_p(\mathbf{x}, \mathbf{w})}{\partial \mathbf{w}} = \left[\frac{\partial \mathbf{h}_p}{\partial l}, \frac{\partial \mathbf{h}_p}{\partial \mathbf{a}}, \frac{\partial \mathbf{h}_p}{\partial \mathbf{b}} \right] \quad (14)$$

$$\mathbf{J}_x \triangleq \frac{\partial \mathbf{h}_p(\mathbf{x}, \mathbf{w})}{\partial \mathbf{x}} = \left[\frac{\partial {}^1p_x(l)}{\partial t}, \frac{\partial {}^1p_z(l)}{\partial t}, \frac{\partial \theta_e|_{(s=l)}}{\partial t} \right]^\top \quad (15)$$

where details of their expressions are in Appendix A and B.

C. Recursive Estimation for State \mathbf{x} and Parameters \mathbf{w}

In this work, we aim at developing a recursive estimation method for both the robot state \mathbf{x} and the shape parameters \mathbf{w} . Both \mathbf{x} and \mathbf{w} are time-variant and subject to noise and disturbance. We use Figure 4 to illustrate the complex and interesting behaviors between \mathbf{x} and \mathbf{w} .

The state \mathbf{x} specifies the level of bending within a homotopy of curves. For example, in Fig. 4, all robot states are chosen to be the same as $\mathbf{x} = 0.5$, indicating that the actuation control action is provided for a middle level bending.

The parameters \mathbf{w} govern the characteristics of different homotopies as the boundaries. The three homotopies shown in Fig. 4 indicate that they are under different loading conditions. We hypothesize that the different external loading will govern the boundaries of different homotopies, shown as green, red, and black in the figure. For instance, in [4], the proposed calibration method by the authors was meant for free-space motion, and as a result, the parameters \mathbf{w} were treated as constants. In this work, we estimate the parameters \mathbf{w} as time-variant, and we envision that such dynamic recursive estimation can unlock potential future method in predicting physical interactions from \mathbf{w} .

Leveraging the kinematics model and the measurement model developed in earlier sections, we choose to implement Extended Kalman Filters (EKF) to facilitate the estimation of both \mathbf{x} and \mathbf{w} , since EKF is an efficient recursive estimation method for generating maximum-likelihood estimates of variables of a non-linear dynamical system. In addition, to support the simultaneous parallel robust estimation of both \mathbf{x} and \mathbf{w} , we choose to use a dual EKF scheme. The details of the dual EKF design are discussed in details in the next section.

IV. DUAL EXTENDED KALMAN FILTER DESIGN

The schematic of the dual EKF scheme is shown in Fig. 5, supported by the nomenclature defined in Table II. The process comprises two filters running concurrently for adapting the state \mathbf{x} and the parameters \mathbf{w} with information exchanged between the two filters. Both the state and the parameters are

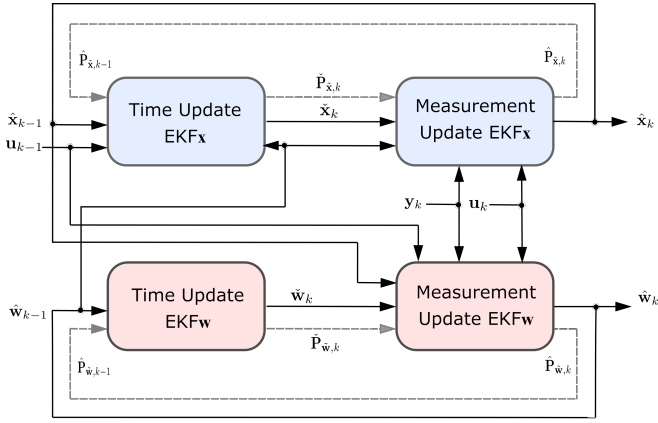


Fig. 5: Schematic of dual EKF scheme for shape parameter and state estimation

estimated based on noisy measurement observations. At each time step k , the state EKF (denoted as EKF_X) estimates the state using the parameter estimate \hat{w}_{k-1} from time step $k-1$, while the parameter EKF (denoted as EKF_W) estimates the parameter using the state estimate \hat{x}_{k-1} from time step $k-1$.

Using the kinematics model and the dual EKF scheme, we build the state dynamic models as:

$$\mathbf{x}_k = \mathbf{x}_{k-1} + \mathbf{u}_{k-1} + \mathbf{v}_{k-1} \quad (16)$$

$$\mathbf{y}_k = \mathbf{h}_p(\mathbf{x}_k, \mathbf{w}_{k-1}) + \mathbf{n}_k \quad (17)$$

where \mathbf{x}_k indicates the state at time step k , \mathbf{h}_p represents the measurement model function derived in III-B, \mathbf{y}_k is the measurement at time step k , \mathbf{u}_{k-1} designates the state process input at time step $k-1$, \mathbf{v}_{k-1} and \mathbf{n}_k are independent Gaussian noise processes with means $\bar{\mathbf{v}}$ and $\bar{\mathbf{n}}$, and covariance matrices $\mathbf{Q}_{\bar{\mathbf{v}}}$ and $\mathbf{R}_{\bar{\mathbf{n}}}$, respectively.

The parameter dynamic model is

$$\mathbf{w}_k = \mathbf{w}_{k-1} + \mathbf{r}_{k-1} \quad (18)$$

$$\mathbf{y}_k = \mathbf{h}_p(\mathbf{x}_{k-1}, \mathbf{w}_k) + \mathbf{e}_k \quad (19)$$

where \mathbf{w}_k indicates the parameter at time step k , \mathbf{r}_{k-1} and \mathbf{e}_k are independent Gaussian noise processes with means $\bar{\mathbf{r}}$ and $\bar{\mathbf{e}}$, and covariance matrices $\mathbf{Q}_{\bar{\mathbf{r}}}$ and $\mathbf{R}_{\bar{\mathbf{e}}}$, respectively.

The dual EKF algorithm is shown in Algorithm 1. The input dataset is the simulated measurements \mathbf{y}_k and state control input \mathbf{u}_k . To avoid lag error and divergence, the initial process noises $\mathbf{Q}_{\bar{\mathbf{v}}}$ and $\mathbf{Q}_{\bar{\mathbf{r}}}$, and measurement noises $\mathbf{R}_{\bar{\mathbf{n}}}$ and $\mathbf{R}_{\bar{\mathbf{e}}}$ need to be initialized properly. After the initialization of $\hat{\mathbf{x}}_0$ and $\hat{\mathbf{w}}_0$ with their covariance matrices $\hat{\mathbf{P}}_{\mathbf{x}_0}$ and $\hat{\mathbf{P}}_{\mathbf{w}_0}$, the dual EKF scheme starts run recurrently. In the *time update* stages, the dual EKF algorithm employ the state dynamic model and parameter dynamic model to propagate the state and the parameter estimates with their covariance matrices, separately. Then, in the *measurement update* stages, we define $\mathbf{K}_{\mathbf{x}_k}$ and $\mathbf{K}_{\mathbf{w}_k}$ as the state Kalman gain and the parameter Kalman gain based on the measurement matrices. The two Kalman gains are used to update both the state and the parameter estimates.

TABLE II: EKF nomenclature and values used in simulation

Symbol	Description	Value used in Simulations
L_0	backbone length	60 mm
ν_r	simulated position noise	0.5 mm
ν_ψ	simulated bending angle noise	1°
\hat{l}_0	initial sensor location	60 mm
$\hat{\mathbf{a}}_0$	initial modal factor vector	$[-0.05/L_0, -0.01/L_0]^\top$
$\hat{\mathbf{b}}_0$	initial modal factor vector	$[-0.5/L_0, -0.15/L_0]^\top$
$\hat{\mathbf{w}}_0$	initial estimated parameter	$[\hat{l}_0, \hat{\mathbf{a}}_0^\top, \hat{\mathbf{b}}_0^\top]^\top$
$\hat{\mathbf{x}}_0$	initial estimated state	0
\mathbf{u}_0	initial state process input	0
$\hat{\mathbf{P}}_{\mathbf{x}_0}$	initial state covariance	0.0001
$\hat{\mathbf{P}}_{\mathbf{w}_0}$	initial parameter covariance	$\text{diag}(0.1, 4e-7, 0.01, 0.0009)$
$\mathbf{Q}_{\bar{\mathbf{v}}}$	state process covariance	0.0001
$\mathbf{Q}_{\bar{\mathbf{r}}}$	parameter process covariance	$\text{diag}(0.01, 0, 0, 0, 0)$
$\mathbf{R}_{\bar{\mathbf{n}}}$	state measurement covariance	$\text{diag}(0.5, 0.5, 0.0006)$
$\mathbf{R}_{\bar{\mathbf{e}}}$	parameter measurement covariance	$\text{diag}(0.25, 0.25, 0.0003)$

The measurement matrices $\mathbf{H}_{\mathbf{x}_k}$ and $\mathbf{H}_{\mathbf{w}_k}$ can be obtained as:

$$\mathbf{H}_{\mathbf{x}_k} = \frac{\partial \mathbf{h}_p(\mathbf{x}, \hat{\mathbf{w}}_{k-1})}{\partial \mathbf{x}} \Big|_{\mathbf{x}=\hat{\mathbf{x}}_k} \quad (20)$$

$$\mathbf{H}_{\mathbf{w}_k} = \frac{\partial \mathbf{h}_p(\hat{\mathbf{x}}_{k-1}, \mathbf{w})}{\partial \mathbf{w}} \Big|_{\mathbf{w}=\hat{\mathbf{w}}_k} \quad (21)$$

where the Jacobian matrices (gradients) above can be found in (14), (15), (17) and (19).

In practice, to improve the accuracy and converging rate on estimates of \mathbf{w} , we use the equation below for $\mathbf{H}_{\mathbf{w}_k}$ in order to take into consideration of internal effects in between \mathbf{x} and \mathbf{w} :

$$\begin{aligned} \mathbf{H}_{\mathbf{w}_k} &= \frac{d\mathbf{h}_p(\hat{\mathbf{x}}_{k-1}, \mathbf{w})}{d\mathbf{w}} \Big|_{\mathbf{w}=\hat{\mathbf{w}}_k} \\ &= \left(\frac{\partial \mathbf{h}_p(\hat{\mathbf{x}}_{k-1}, \mathbf{w})}{\partial \mathbf{w}} + \frac{\partial \mathbf{h}_p(\hat{\mathbf{x}}_{k-1}, \mathbf{w})}{\partial \hat{\mathbf{x}}_{k-1}} \frac{d\hat{\mathbf{x}}_{k-1}}{d\mathbf{w}} \right) \Big|_{\mathbf{w}=\hat{\mathbf{w}}_k} \end{aligned} \quad (22)$$

where the derivation of $\frac{d\mathbf{x}}{d\mathbf{w}}$ can be found in Appendix C.

V. SIMULATION

To evaluate the feasibility and performance of the proposed shape estimation method, we conduct simulation studies programmed in *Python* environment following the workflow in Fig. 6, which includes a parameter generation module, a measurement data generation module and a dual EKF scheme module.

Algorithm 1 Dual EKF Estimation

Input: $\mathcal{D}\{y_k, u_k\}$, $k=1, \dots, N$; $Q_{\bar{v}}$; $R_{\bar{n}}$; $Q_{\bar{r}}$; and $R_{\bar{e}}$

- 1: **START** Initialize: $\hat{x}_0, u_0, \hat{P}_{x_0}$ and \hat{w}_0, \hat{P}_{w_0}
- 2: **for** $k = 1$ to N **do**
- 3: **State time update:**
- 4: $\check{x}_k = \hat{x}_{k-1} + u_{k-1}$, $\check{P}_{x_k} = \hat{P}_{x_{k-1}} + Q_{\bar{v}}$,
- 5: **Parameter time update:**
- 6: $\check{w}_k = \hat{w}_{k-1}$, $\check{P}_{w_k} = \hat{P}_{w_{k-1}} + Q_{\bar{r}}$
- 7: **State measurement update:**
- 8: Compute H_{x_k} from (20)
- 9: $K_{x_k} = \check{P}_{x_k} H_{x_k}^T (H_{x_k} \check{P}_{x_k} H_{x_k}^T + R_{\bar{n}})^{-1}$
- 10: $\hat{x}_k = \check{x}_k + K_{x_k} (y_k - H_{x_k} \check{x}_k)$
- 11: $\hat{P}_{x_k} = (I - K_{x_k} H_{x_k}) \check{P}_{x_k}$
- 12: **Parameter measurement update:**
- 13: Compute H_{w_k} from (22)
- 14: $K_{w_k} = \check{P}_{w_k} H_{w_k}^T (H_{w_k} \check{P}_{w_k} H_{w_k}^T + R_{\bar{e}})^{-1}$
- 15: $\hat{w}_k = \check{w}_k + K_{w_k} (y_k - H_{w_k} \check{w}_k)$
- 16: $\hat{P}_{w_k} = (I - K_{w_k} H_{w_k}) \check{P}_{w_k}$
- 17: **end for**

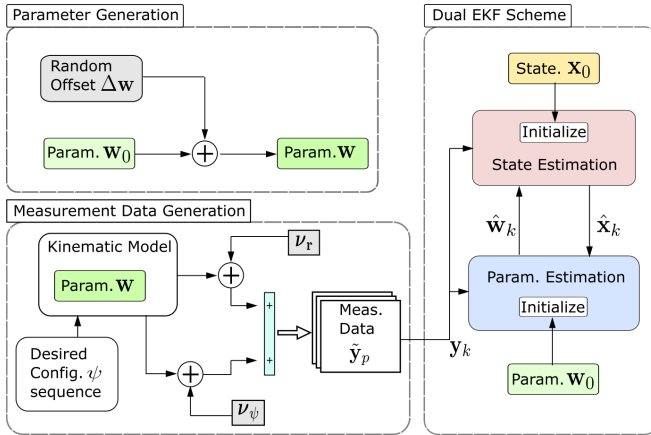


Fig. 6: Simulation workflow

A. Workflow

In the *parameter generation module*: given a nominal shape parameter w_0 , a random offset Δw is applied to result in an actual shape parameter vector w .

In the *measurement data generation module*: the vector w is then used for generating simulated tip position and orientation measurements via the kinematics model. Specifically, we select 500 evenly spaced t values between 0 and 1 as the desired configuration space sequence to generate 500 consecutive simulated measurement data samples. These samples are prepared to be fed continuously into the estimation framework to consume. For the finalized noisy measurements \tilde{y}_p , we also add position noise vector ν_r and orientation noise vector ν_ψ .

We engineer the following state process input u_k for time step k , taking intuition from (5):

$$u_k = (\check{\theta}_{e_k} - \check{\theta}_{e_{k-1}}) / (\tilde{\theta}_{e_b} - \tilde{\theta}_{e_a}) \quad (23)$$

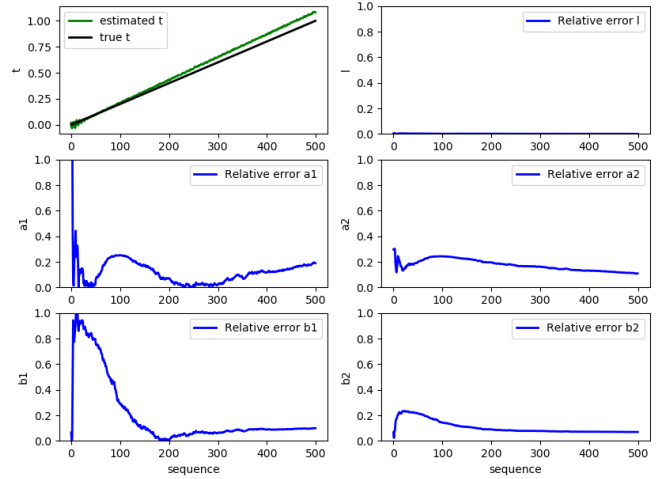


Fig. 7: State estimate and relative errors of parameter estimates comparing to true values

where $\check{\theta}_{e_k}$ and $\check{\theta}_{e_{k-1}}$ are the end effector bending angles predicted through the kinematics model using predicted state at time step k and $k-1$. The angles $\tilde{\theta}_{e_b}$ and $\tilde{\theta}_{e_a}$ designate the measured most bent bending angle and the measured least bent bending angle, as depicted in Fig. 2(a), respectively.

The *dual EKF scheme module* run recurrently to correct the predicted state and parameters sequentially using the continuously fed simulated data samples y_k drawn from the noisy measurements \tilde{y}_p . All related initial parameter settings about the simulation study are given in Table II.

B. Results

In the dual EKF scheme module, the estimates of the state and the parameters are recorded at each time step. We capture the relative errors¹ between the parameter estimates and their true values over all sequence. The estimation results of state and parameters are shown in Fig. 7. The nontrivial part of Kalman filter tuning is to reduce lag and to minimize noise.

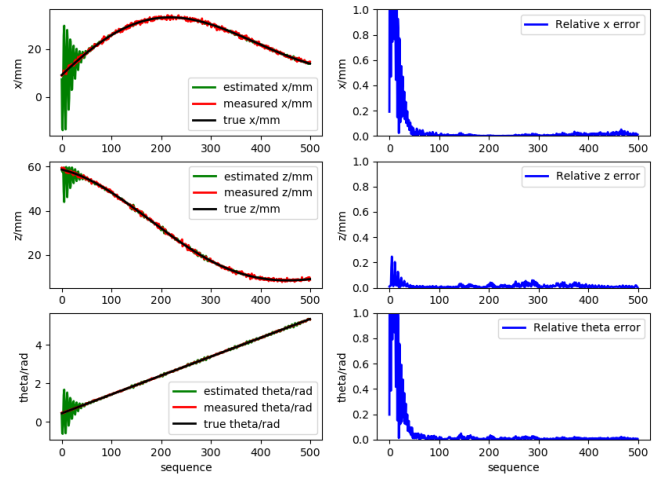


Fig. 8: x, z coordinates and θ_e estimation with their relative errors comparing to true values

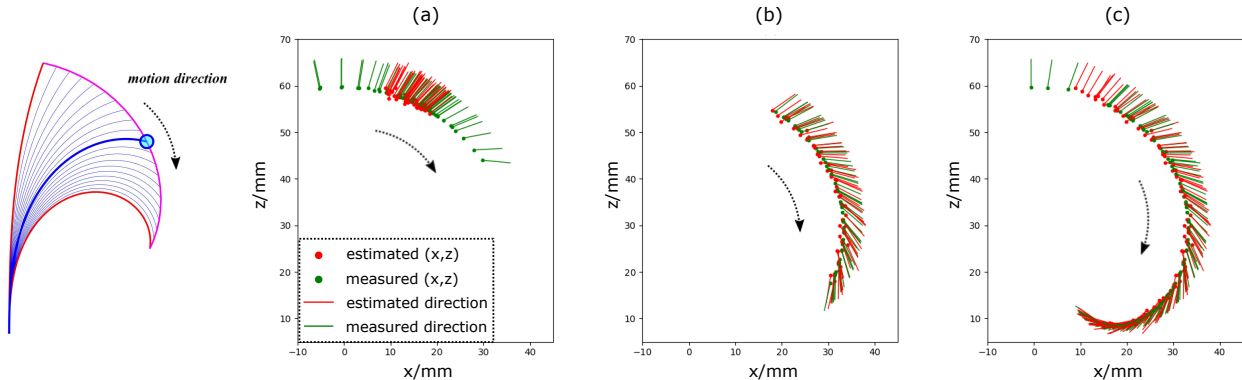


Fig. 9: Illustration of pose estimates and measurements: (a) sequence from 1 to 50, (b) sequence from 51 to 300, (c) sequence from 1 to 500.

By adopting the initialization numeric values reported in Table II, we obtain promising outcomes. Over time, the state estimates can track the true value responsively with small overshoot after the initial phase, and the parameter estimates can converge accurately.

To evaluate the residual error performance of proposed estimation scheme, we compare the predicted position and bending angle with the measured and true values separately, and calculate their relative errors with respect to the true values. The result is reported in Fig. 8. The same result is visualized in Fig. 9 in a more intuitive manner, where the tip positions and orientations are plotted, for the estimated and the measured, respectively.

Figure 8 and Figure 9 both show a robust estimation behavior of the dual EKF: after an initial uncertain phase (about 50 samples), the position and bending angle prediction become stable and accurate.

While the dual EKF algorithm proposed in this work performs well in estimating the robot state and the parameters simultaneously, we believe the algorithm has the potential for more accurate estimation. The additional tuning of noise parameters may be helpful in performance improvement. The deployment of hardware experimental validation can also show insights for potential improvements.

VI. CONCLUSION AND FUTURE WORK

In this work, we develop and present an online shape estimation method to simultaneously estimate the robot state and the shape parameters of continuum robots. We leverage modal parameterization for decoupling the state and the parameters, and we adapt a dual Extended Kalman Filter for recursive estimation. We conducted simulation studies to evaluate the performance of the dual EKF implementation. The developed dual EKF demonstrated recurrent operation that consumes continuous simulated measurement data. The results indicate promising capability of the proposed method to accurately estimate both the robot state and shape parameters.

The planned future work includes:

¹The relative error is defined as $e = |(v_{\text{est}} - v_{\text{true}})/v_{\text{true}}|$

- Extend to conduct more rigorous simulation studies for dynamically changing parameter trajectories
- Extend to accommodate 6-Dimensional pose measurements at multiple locations in order to support applicable hardware experimental validation.
- Conduct experimental validation on a continuum robot hardware platform.
- Investigate potential approach to predict physical interaction from the shape estimates.

APPENDIX

A. Derivation of \mathbf{J}_w

$$\mathbf{J}_w = \frac{\partial \mathbf{h}_p(\mathbf{x}, \mathbf{w})}{\partial \mathbf{w}} = \left[\frac{\partial \mathbf{h}_p}{\partial l}, \frac{\partial \mathbf{h}_p}{\partial \mathbf{a}}, \frac{\partial \mathbf{h}_p}{\partial \mathbf{b}} \right] \quad (24)$$

$$\frac{\partial \mathbf{h}_p}{\partial l} = [s_{\theta_s}(l), c_{\theta_s}(l), \kappa(l)]^\top \quad (25)$$

$$\frac{\partial \mathbf{h}_p}{\partial \mathbf{a}} = (1-t) \int_0^l \left[\begin{array}{c} [-c_{\theta_s}, s_{\theta_s}]^\top \boldsymbol{\nu}^\top \\ \boldsymbol{\eta}^\top \end{array} \right] ds \quad (26)$$

$$\frac{\partial \mathbf{h}_p}{\partial \mathbf{b}} = t \int_0^l \left[\begin{array}{c} [-c_{\theta_s}, s_{\theta_s}]^\top \boldsymbol{\nu}^\top \\ \boldsymbol{\eta}^\top \end{array} \right] ds \quad (27)$$

$$\boldsymbol{\nu}(s) = \int_0^s \boldsymbol{\eta}(\tau) d\tau = \left[\begin{array}{c} s \\ \frac{s}{2} \end{array} \right] \boldsymbol{\eta}(s) \quad (28)$$

$$\boldsymbol{\eta}(s) = [1, s^1]^\top \quad (29)$$

B. Derivation of \mathbf{J}_x

$$\begin{aligned} \mathbf{J}_x &= \frac{\partial \mathbf{h}_p(\mathbf{x}, \mathbf{w})}{\partial \mathbf{x}} = \frac{\partial \mathbf{h}_p}{\partial t} \\ &= \left[\frac{\partial^1 x(l)}{\partial t}, \frac{\partial^1 z(l)}{\partial t}, \frac{\partial \theta_s|_{(s=l)}}{\partial t} \right]^\top \end{aligned} \quad (30)$$

$$\frac{\partial^1 x(l)}{\partial t} = \int_0^l \left(c_{\theta_s} \frac{\partial}{\partial t} \theta_s(s) \right) ds \quad (31)$$

$$\frac{\partial^1 z(l)}{\partial t} = \int_0^l \left(-s_{\theta_s} \frac{\partial}{\partial t} \theta_s(s) \right) ds \quad (32)$$

$$\frac{\partial}{\partial t} \theta_s(s) = \int_0^s [\kappa_b(\tau) - \kappa_a(\tau)] d\tau \quad (33)$$

C. Derivation of $\frac{dx}{dw}$

Referring to (5) and 7, we can obtain:

$$x = t = \frac{\theta_e - \theta_{e_a}}{\theta_{e_b} - \theta_{e_a}} \quad (34)$$

$$\frac{dx}{dw} = \frac{\partial t}{\partial \theta_e} \frac{d\theta_e}{dw} + \frac{\partial t}{\partial \theta_{e_a}} \frac{d\theta_{e_a}}{dw} + \frac{\partial t}{\partial \theta_{e_b}} \frac{d\theta_{e_b}}{dw} \quad (35)$$

REFERENCES

- [1] S. Hirose, "Biologically inspired robots," *Snake-Like Locomotors and Manipulators*, 1993.
- [2] N. Simaan, R. M. Yasin, and L. Wang, "Medical technologies and challenges of robot-assisted minimally invasive intervention and diagnostics," *Annual Review of Control, Robotics, and Autonomous Systems*, vol. 1, pp. 465–490, 2018.
- [3] P. E. Dupont, N. Simaan, H. Choset, and C. Rucker, "Continuum robots for medical interventions," *Proceedings of the IEEE*, vol. 110, no. 7, pp. 847–870, 2022.
- [4] L. Wang and N. Simaan, "Geometric calibration of continuum robots: Joint space and equilibrium shape deviations," *IEEE Transactions on Robotics*, vol. 35, no. 2, pp. 387–402, 2019.
- [5] N. Simaan, R. Taylor, and P. Flint, "A dexterous system for laryngeal surgery," in *IEEE International Conference on Robotics and Automation, 2004. Proceedings. ICRA'04. 2004*, vol. 1. IEEE, 2004, pp. 351–357.
- [6] P. Sears and P. Dupont, "A Steerable Needle Technology Using Curved Concentric Tubes," in *2006 IEEE/RSJ International Conference on Intelligent Robots and Systems*. Beijing, China: IEEE, oct 2006, pp. 2850–2856.
- [7] D. B. Camarillo, C. F. Milne, C. R. Carlson, M. R. Zinn, and J. K. Salisbury, "Mechanics modeling of tendon-driven continuum manipulators," *IEEE transactions on robotics*, vol. 24, no. 6, pp. 1262–1273, 2008.
- [8] R. J. Webster III and B. A. Jones, "Design and kinematic modeling of constant curvature continuum robots: A review," *The International Journal of Robotics Research*, vol. 29, no. 13, pp. 1661–1683, 2010.
- [9] M. W. Hannan and I. D. Walker, "Kinematics and the implementation of an elephant's trunk manipulator and other continuum style robots," *Journal of robotic systems*, vol. 20, no. 2, pp. 45–63, 2003.
- [10] "A Modular Open-Source Continuum Manipulator for Underwater Remotely Operated Vehicles," vol. 14, no. 6, pp. 1–10, dec 2022.
- [11] Q. Zhao, G. Zhang, H. Jafarnejadsani, and L. Wang, "A modular continuum manipulator for aerial manipulation and perching," *arXiv preprint arXiv:2206.06246*, 2022.
- [12] R. E. Goldman, A. Bajo, and N. Simaan, "Compliant Motion Control for Multisegment Continuum Robots With Actuation Force Sensing," *IEEE Transactions on Robotics*, pp. 1–13, 2014.
- [13] I. S. Godage, G. A. Medrano-Cerda, D. T. Branson, E. Guglielmino, and D. G. Caldwell, "Modal kinematics for multisegment continuum arms," *Bioinspiration & biomimetics*, vol. 10, no. 3, p. 035002, 2015.
- [14] G. S. Chirikjian and J. W. Burdick, "A modal approach to hyper-redundant manipulator kinematics," *IEEE Transactions on Robotics and Automation*, vol. 10, no. 3, pp. 343–354, 1994.
- [15] L. Wang and N. Simaan, "Investigation of Error Propagation in Multi-backbone Continuum Robots," in *Advances in Robot Kinematics*. Cham: Springer International Publishing, 2014, pp. 385–394.
- [16] S. Song, Z. Li, M. Q. Meng, H. Yu, and H. Ren, "Real-Time Shape Estimation for Wire-Driven Flexible Robots With Multiple Bending Sections Based on Quadratic Bézier Curves," *IEEE Sensors Journal*, vol. 15, no. 11, pp. 6326–6334, nov 2015.
- [17] S. Song, Z. Li, H. Yu, and H. Ren, "Shape reconstruction for wire-driven flexible robots based on Bézier curve and electromagnetic positioning," *Mechatronics*, vol. 29, pp. 28–35, aug 2015.
- [18] C. Shi, X. Luo, P. Qi, T. Li, S. Song, Z. Najdovski, T. Fukuda, and H. Ren, "Shape sensing techniques for continuum robots in minimally invasive surgery: A survey," *IEEE Transactions on Biomedical Engineering*, vol. 64, no. 8, pp. 1665–1678, 2017.
- [19] H. Bezwada, C. Woods, and V. Vikas, "Shape Estimation of Soft Manipulators using Piecewise Continuous Pythagorean-Hodograph Curves," in *2022 American Control Conference (ACC)*. IEEE, jun 2022, pp. 2905–2910.
- [20] ———, "Shape Reconstruction of Soft Manipulators Using Vision and IMU Feedback," *IEEE Robotics and Automation Letters*, vol. 7, no. 4, pp. 9589–9596, 2022.
- [21] B. A. Jones, R. L. Gray, and K. Turlapati, "Three dimensional statics for continuum robotics," in *2009 IEEE/RSJ International Conference on Intelligent Robots and Systems*. IEEE, 2009, pp. 2659–2664.
- [22] J. Till, V. Alois, and C. Rucker, "Real-time dynamics of soft and continuum robots based on cosserat rod models," *The International Journal of Robotics Research*, vol. 38, no. 6, pp. 723–746, 2019.
- [23] F. Boyer, V. Lebastard, F. Candelier, and F. Renda, "Dynamics of continuum and soft robots: A strain parameterization based approach," *IEEE Transactions on Robotics*, vol. 37, no. 3, pp. 847–863, 2020.
- [24] F. Renda, F. Boyer, J. Dias, and L. Seneviratne, "Discrete Cosserat Approach for Multisection Soft Manipulator Dynamics," *IEEE Transactions on Robotics*, vol. 34, no. 6, pp. 1518–1533, dec 2018.
- [25] D. C. Rucker and R. J. Webster III, "Statics and dynamics of continuum robots with general tendon routing and external loading," *IEEE Transactions on Robotics*, vol. 27, no. 6, pp. 1033–1044, 2011.
- [26] S. Huang, D. Meng, X. Wang, B. Liang, and W. Lu, "A 3d static modeling method and experimental verification of continuum robots based on pseudo-rigid body theory," in *2019 IEEE/RSJ International Conference on Intelligent Robots and Systems (IROS)*. IEEE, 2019, pp. 4672–4677.
- [27] H.-J. Su, "A Pseudorigid-Body 3R Model for Determining Large Deflection of Cantilever Beams Subject to Tip Loads," *Journal of Mechanisms and Robotics*, vol. 1, no. 2, 01 2009, 021008.
- [28] M. Khoshnam, I. Khalaji, and R. V. Patel, "A robotics-assisted catheter manipulation system for cardiac ablation with real-time force estimation," in *2015 IEEE/RSJ International Conference on Intelligent Robots and Systems (IROS)*. IEEE, 2015, pp. 3202–3207.
- [29] R. J. Roesthuis and S. Misra, "Steering of multisegment continuum manipulators using rigid-link modeling and fbg-based shape sensing," *IEEE transactions on robotics*, vol. 32, no. 2, pp. 372–382, 2016.
- [30] A. Bajo and N. Simaan, "Kinematics-Based Detection and Localization of Contacts Along Multisegment Continuum Robots," *IEEE Transactions on Robotics*, vol. 28, no. 2, pp. 291–302, apr 2012.
- [31] Y. Chen, L. Wang, K. Galloway, I. Godage, N. Simaan, and E. Barth, "Modal-Based Kinematics and Contact Detection of Soft Robots," *Soft Robotics*, p. soro.2019.0095, jul 2020.
- [32] Q. Qiao, G. Borghesan, J. De Schutter, and E. Vander Poorten, "Force from shape—estimating the location and magnitude of the external force on flexible instruments," *IEEE Transactions on Robotics*, vol. 37, no. 5, pp. 1826–1833, 2021.